

Equivalent Circuit Modeling of Mutually Resistively Coupled Microwave Cavities with Enhanced Phase Sensitivity Using Thin Metallic Foils

Michael T. Hatzon,^{1,*} Graeme R. Flower,¹ Robert C. Crew,¹ Jeremy F. Bourhill,¹ and Michael E. Tobar¹

¹*Quantum Technologies and Dark Matter Research Lab, Department of Physics,
University of Western Australia, Crawley, WA 6009, Australia*

(Dated: March 6, 2026)

We formulate and validate an equivalent circuit model describing mutual resistive coupling between three microwave cavity resonators interconnected via thin metallic foils. Each cavity is represented as a lumped LCR circuit, while the foils act as a dissipative interface that mediates energy exchange via mutual resistance. This coupling mechanism produces interference effects and a controllable anti-resonance when the input resonators are amplitude- and phase-balanced, a behavior not achievable with standard microwave antenna probes. All three resonators operated in the TM_{010} mode, where two input resonators each excited the third via a thin copper foil. Analytical expressions are derived for the mutual resistance and coupling coefficient of these foils in this geometry. Under balanced conditions, a sharp anti-resonance emerges with a near order-of-magnitude enhanced phase sensitivity at the resonant frequency of the output cavity, consistent with model predictions. The experimentally extracted mutual coupling coefficients, $\Delta_{13} = (5.00 \pm 0.01) \times 10^{-6}$ and $\Delta_{23} = (4.10 \pm 0.01) \times 10^{-6}$, fall within the calculated range $\Delta_{n,3} \approx (1-48) \times 10^{-6}$ derived from the foil's electromagnetic properties, where the spread is dominated by the estimated foil thickness uncertainty of $(9 \pm 1) \mu\text{m}$. These results confirm that resistive coupling can occur across a number of skin depths of a metallic interface, providing a new means of engineering controlled interference in multi-resonator systems. The approach offers potential applications in precision microwave experiments, phase-sensitive detection, and tests of fundamental electromagnetic interactions.

I. INTRODUCTION

Microwave cavity resonators are foundational components in precision measurement systems [1], frequency standards [2], and emerging quantum technologies [3–5]. Their ability to confine and sustain electromagnetic fields with extremely high quality factors makes them indispensable for experiments requiring long coherence times and minimal dissipation [6]. Such resonators underpin a wide range of applications, including dielectric and material-loss characterization [7–9], high-resolution spectroscopy [10–13], cavity electromechanical [14–16], and precision frequency control [17]. They also serve as key elements in quantum devices, hybrid photonic-microwave systems, and precision tests of fundamental physics, where stability and phase coherence are paramount [18, 19].

The way in which two or more resonators are coupled governs the exchange of energy and phase information between them, determining the collective response of the system [20]. Controlled coupling enables a rich variety of interference effects, including linewidth narrowing, normal-mode splitting, mode hybridization, or sharp anti-resonances [21–24]. By engineering the strength and phase of inter-resonator coupling, one can tailor the spectral response of the system for specific measurement or filtering purposes, as well as create conditions for coherent cancellation and enhanced sensitivity.

Coupled-resonator systems are conventionally realized through shared inductive or capacitive elements, or via

aperture-mediated coupling mechanisms [10], each producing reactive interactions that modify the system's collective resonance response. Resistive coupling, by contrast, has typically been regarded as a loss mechanism rather than a deliberate means of inter-resonator interaction. Some methods have been developed that invoke resistive coupling, including microwave filter networks [25], power-line communication systems [26], and cavity resonances coupling to line resonance due to a finite voltage standing wave ratio (VSWR) [27], though these are generally confined to planar or lumped-element implementations. To our knowledge, mutual resistive coupling between 3D microwave cavity resonators, realized here, has not been systematically investigated as a standalone coupling mechanism.

The motivation for this study arises from a three-cavity microwave system previously developed for tests of the scalar Electric Aharonov-Bohm effect [28, 29], in which two input cavities drove a third output cavity through thin copper foils many skin depths thick. When tuned, the system exhibited sharp anti-resonances with a strong dependence on the relative input phase.

Building upon these observations, we enhanced the readout sensitivity and developed an analytical model of the three-cavity system (Fig. 1) by introducing mutual resistance terms [27] to describe coupling through the foils. Each cavity is represented as a lumped LCR resonator, with resistive inter-cavity terms proportional to the dissipative power transferred across the interface. The model reproduces the observed interference and anti-resonant behaviour and is complemented by a first-principles derivation relating the foil's electromagnetic properties to the measured coupling.

* michael.hatzon@uwa.edu.au

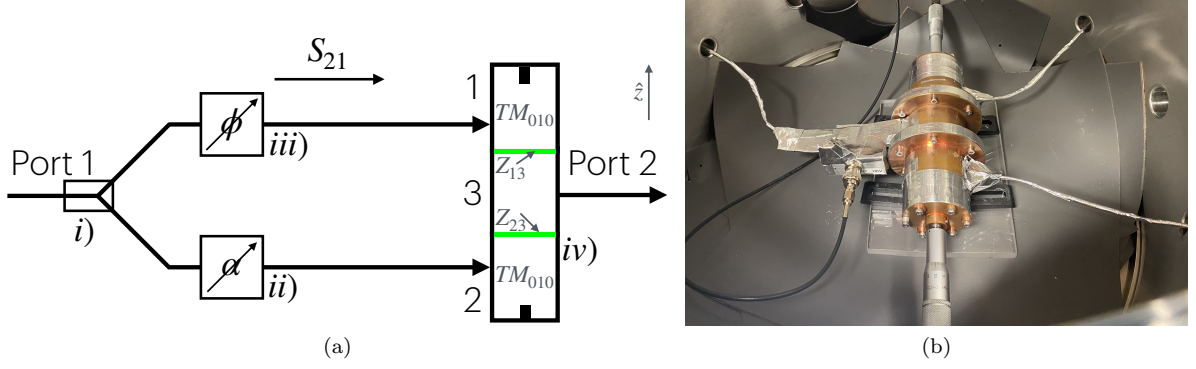


FIG. 1. (a) The experimental configuration used to excite a sharp anti-resonance. The vector network analyser (VNA) signal entered from Port 1 and is split into two signals via a 3dB power splitter, labelled i). One signal passes through ii) a variable attenuator, acquiring a relative attenuation factor α . The other passes through iii) a microwave phase shifter, introducing a relative phase shift ϕ between the two signals. The two signals excite iv) the three-cavity system, where the TM_{010} mode of resonators 1 and 2 was excited, and each resonator coupled to resonator 3 through a $<10\ \mu\text{m}$ thick copper foil. The coupling between resonators 1–3 and 2–3 is represented by the mutual impedances Z_{13} and Z_{23} , respectively, which can be approximated as mutual resistances R_{13} and R_{23} near resonance. Port 2 has three series output amplifiers (two Low Noise Factory ≈ 37 dB and Minicircuits 17 dB) totaling 89.7 dB of gain in the circuit. (b) Photograph of the fabricated three-cavity apparatus with shielding. The interferometric input and the remaining two output amplifiers are located outside the chamber.

This work establishes a new coupling mechanism between volumetric microwave resonators, arising purely from resistive dissipation across a conductive interface. The framework provides both experimental and analytical foundations for resistive coupling in microwave resonators, enabling controlled anti-resonances and balance conditions useful for interferometric precision measurements and tests of fundamental physics.

II. EQUIVALENT CIRCUIT MODEL

An equivalent circuit representation of the experimental system is shown in Fig. 2. Each of the three resonators in Fig. 1a is modelled as an LCR circuit characterised by its resonance frequency f_n , quality factor Q_n , and probe coupling coefficients β_n . The conductive foils separating the cavities introduce mutual resistive terms, R_{13} and R_{23} , corresponding to the dissipative current flow between the input and output resonators.

The transfer function, T , of the system is defined as

$$T = \frac{I_{out}}{I_{in}}, \quad (1)$$

where phasors I_{in} is the Thevenin equivalent input current at port 1, and I_{out} is the current dissipated across the port 2 (resonator 3) output resistor. Under matched impedance conditions, this quantity is proportional to the forward transmission coefficient of the microwave circuit, S_{21} , and therefore represents the measured complex transmission response. The input current is split into I_1 and I_2 , and a relative phase, ϕ , and attenuation, α , is

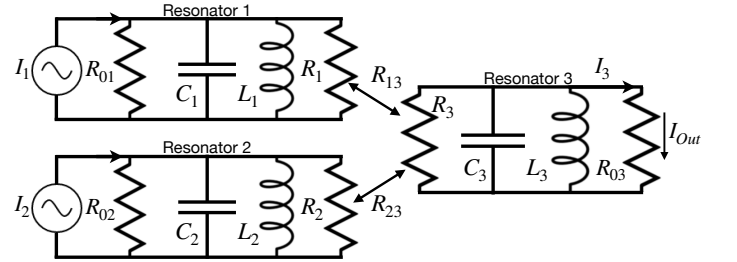


FIG. 2. The equivalent circuit diagram of the three-cavity resonator system coupled through thin metal foils. The three resonators are modelled by standard LCR circuits with capacitance C_n , inductance L_n , resistance R_n , and probe resistances R_{0n} for resonator n . The mutual resistance terms R_{13} and R_{23} , are shown coupling the resonators. The currents entering resonators 1 and 2, are modelled by current sources I_1 and I_2 , with I_3 the current entering resonator 3 due to mutual contributions. The output current I_{out} passes through the third resonator's probe.

introduced between the two new currents, related by

$$I_1 = \frac{1}{\sqrt{2}} I_{in} \quad (2)$$

and

$$I_2 = \frac{1}{\sqrt{2}} \alpha e^{i\phi} I_{in}. \quad (3)$$

Each of the parallel LCR circuits ($n = 1, 2, 3$) has a self admittance of

$$Y_{nn} = \frac{1}{R_{0n}} + \frac{1}{R_n} + i\omega C_n + \frac{1}{i\omega L_n}, \quad (4)$$

with R_{0n} and R_n the probe and resonator resistances, respectively, capacitance C_n , inductance L_n , and angular frequency $\omega = 2\pi f$. Near resonance, one can set $C_n \rightarrow \frac{1}{\omega_n^2 L_n}$, $L_n \rightarrow \frac{R_n}{\omega_n Q_n}$ and $R_n \rightarrow \beta_n R_{0n}$. Taking the power series and excluding terms quadratic and higher in f , the self-admittance becomes

$$Y_{nn} = \frac{1}{\beta_n R_{0n}} (1 + \beta_n + 2iQ_n \frac{f - f_n}{f_n}). \quad (5)$$

The mutual admittances $Y_{13} = Y_{31} = \frac{1}{R_{13}}$ and $Y_{23} = Y_{32} = \frac{1}{R_{23}}$ (simplification justified in Section IV) couple resonators 1–3 and 2–3, respectively, while resonators 1 and 2 remain uncoupled with no mutual foils ($Y_{12} = Y_{21} = 0$). It is here that we can introduce a normalised mutual coupling term Δ with reference to the mutual resistance

$$\Delta_{n3} = \frac{R_{03} \sqrt{\beta_n \beta_3}}{R_{n3}}. \quad (6)$$

Nodal analysis on the equivalent circuit in Fig. 2, gives three simultaneous equations:

$$I_1 = Y_{11}V_1 + Y_{13}V_3, \quad (7a)$$

$$I_2 = Y_{22}V_2 + Y_{23}V_3, \quad (7b)$$

$$0 = Y_{31}V_1 + Y_{32}V_2 + Y_{33}V_3, \quad (7c)$$

for resonators 1, 2 and 3, respectively, with three unknown voltages V_1 , V_2 and V_3 corresponding to each parallel node. Solving Eqs. (7a)–(7c) simultaneously, T can be determined. Written in terms of microwave parameters, it becomes

$$T = \frac{1}{\sqrt{2}} \frac{f_3 \sqrt{\beta_3} (f_1 \sqrt{\beta_1} \gamma_2 \Delta_{13} + e^{i\phi} \alpha f_2 \sqrt{\beta_2} \gamma_1 \Delta_{23})}{-\gamma_1 \gamma_2 \gamma_3 + f_1 \gamma_2 f_3 \Delta_{13}^2 + \gamma_1 f_2 f_3 \Delta_{23}^2}, \quad (8)$$

with the function

$$\gamma_n = -2ifQ_n + f_n(-1 - \beta_n + 2iQ_n), \quad (9)$$

for $n = 1, 2, 3$.

Interesting phenomena arise when the currents through to the output resistor are closely balanced. To determine the balance condition, we set the attenuation factor α acting on I_2 , such that $T = 0$. Under the assumption that all three resonators are tuned to the same resonant frequency ($f_1 = f_2 = f_3$), and that the relative phase is matched, the required attenuation is,

$$\alpha = \frac{\sqrt{\beta_1}(1 + \beta_2)\Delta_{13}}{\sqrt{\beta_2}(1 + \beta_1)\Delta_{23}}. \quad (10)$$

Eq. 10 provides the symmetric-limit intuition; in practice small detunings shift the optimal balance point slightly, which is captured in the full model (Eq. 8) used for fitting.

III. FITTING THE DATA

Three experimental spectra are plotted in Fig. 3 and fitted using the transfer function in Eq. (8) via standard nonlinear least-squares optimisation in Python. All measurements presented here were acquired with improved electromagnetic shielding and a lower-noise amplification chain, resulting in enhanced contrast and signal-to-noise ratio compared to [28, 29]. The resonance frequencies f_1 and f_2 , and probe coupling coefficients β_1 and β_2 , were determined independently from single-resonator characterisation and held fixed during the fit; all remaining parameters were extracted from the optimisation. The relative phase between the two input signals was varied from a case of destructive interference ($\phi = \pi$) to constructive interference ($\phi = 0$). In the destructive case, a sharp cancellation (anti-resonance) feature emerges and the phase slope is enhanced compared to the near-resonant case.

There is good agreement between the model and experiment, with the extracted parameters summarised in Table I. The model reproduces this measured dependence on the relative input phase ϕ : as ϕ is tuned towards the balanced condition, a sharp anti-resonance forms and the phase slope steepens.

Small system asymmetries (e.g., unequal resonance frequencies or Q -factors) create the ideal single anti-resonance when ϕ approaches π , as observed in Fig. 3a. Additional imbalance in α can lead to a splitting of this feature within the nearby phase region. In the symmetric limit, where all relevant parameters are equal, exact cancellation occurs at ($\phi = \pi$) and broadband suppression is recovered across the plotted frequency span.

The central resonator frequency, f_3 , was allowed to vary within a narrow range of approximately ± 30 kHz during the fitting procedure, which is substantially smaller than the resonator bandwidth (of order MHz). This small freedom accounts for slight frequency drift observed during measurements, most likely arising from temperature or pressure fluctuations that becomes visible at the achieved low-noise measurement level. Other than f_3 , only ϕ was allowed to vary over the range and all other parameters were kept constant. The model shows strong agreement with measurements across the full tuning range, as demonstrated in Fig. 4, which compares the measured response with the simulated transfer function as ϕ is swept over approximately π , consistent with the experimentally measured tuning range of 3.00 rad at 6.1 GHz.

The three resonators exhibit comparable quality factors and are only weakly detuned, consistent with the near-symmetric behaviour expected for the balanced interference condition. The fitted mutual coupling coefficients are very small, on the order of 10^{-6} , consistent with the weak interaction expected when the electromagnetic field couples across many skin depths of copper. The small difference between Δ_{13} and Δ_{23} likely arises from variations in surface field distributions, minor geometric asymmetries, or small differences in foil thickness.

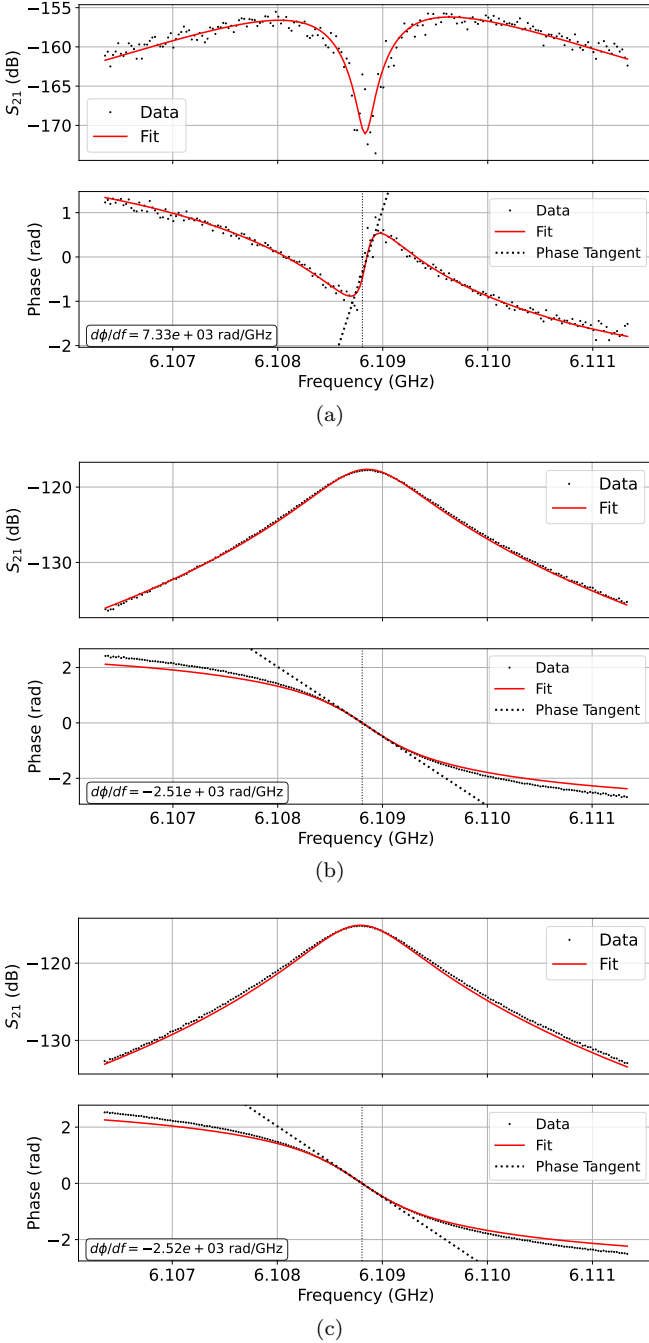


FIG. 3. Magnitude and phase versus frequency, with the best-fit transfer function from Eq. (8) plotted alongside the data. The corresponding fit parameters are listed in Table I. Panels (a)-(c) illustrate the incremental approach towards resonance as the fitted relative phase ϕ is varied from π to near 2π radians, respectively. The input power at port 1 was 20 dBm and the measured S_{21} spectra are referenced to the input of the amplifier chain.

In Section IV, the physical interpretation of this mutual coupling is discussed and an expected value for the coupling rate based on mutual resistance is derived.

To directly measure the phase enhancement, an inde-

TABLE I. System parameters used for the fits in Fig. 3.

Measured parameters	
f_1 (GHz)	6.10883
f_2 (GHz)	6.10886
β_1	0.81
β_2	1.26
Fitted parameters	
f_3 (GHz)	6.10883
Q_1	2.7×10^3
Q_2	3.1×10^2
Q_3	12.2×10^3
Δ_{13}	$(5.00 \pm 0.01) \times 10^{-6}$
Δ_{23}	$(4.10 \pm 0.01) \times 10^{-6}$
α	1.23
β_3	0.93

pendent spectrum in Fig. 5 was acquired by finely tuning the balance parameters (ϕ and α) to approach the destructive condition. This demonstrates a near order-of-magnitude increase in the local phase slope compared with the unbalanced configuration. This provides a direct, data-driven confirmation of the phase enhancement predicted by the model. Though both Fig. 5 and Fig. 3a show the destructive case, small differences in balance parameters can cause the polar plot to circle the origin and give the enhanced phase response in Fig. 5, rather than the inversion seen in Fig. 3a. This is similar to the difference between an under-coupled and over-coupled resonator.

Due to ambient temperature and pressure fluctuations, maintaining the antiresonant condition is experimentally challenging, as the balanced interference point is extremely sensitive to small frequency drifts. Improved thermal and environmental stability, such as operation under vacuum or at cryogenic temperature, is expected to significantly improve the robustness of this operating regime and may be explored in future work.

Having established the phenomenology of the enhancement, we next consider the physical origin of the weak mutual coupling responsible for this behaviour.

IV. COUPLING ACROSS A METALLIC FOIL

A. Derivation

To verify the physical significance of the mutual coupling term Δ_{n3} , and hence the mutual resistance R_{n3} , we derive its value from first principles and compare it with the value obtained from model fitting. First, consider the electric field induced at either side of a thin sheet, \vec{E}_n and \vec{E}_3 , for foil sides n (where n is now either 1 or 2, representing the side of the associated input resonator)

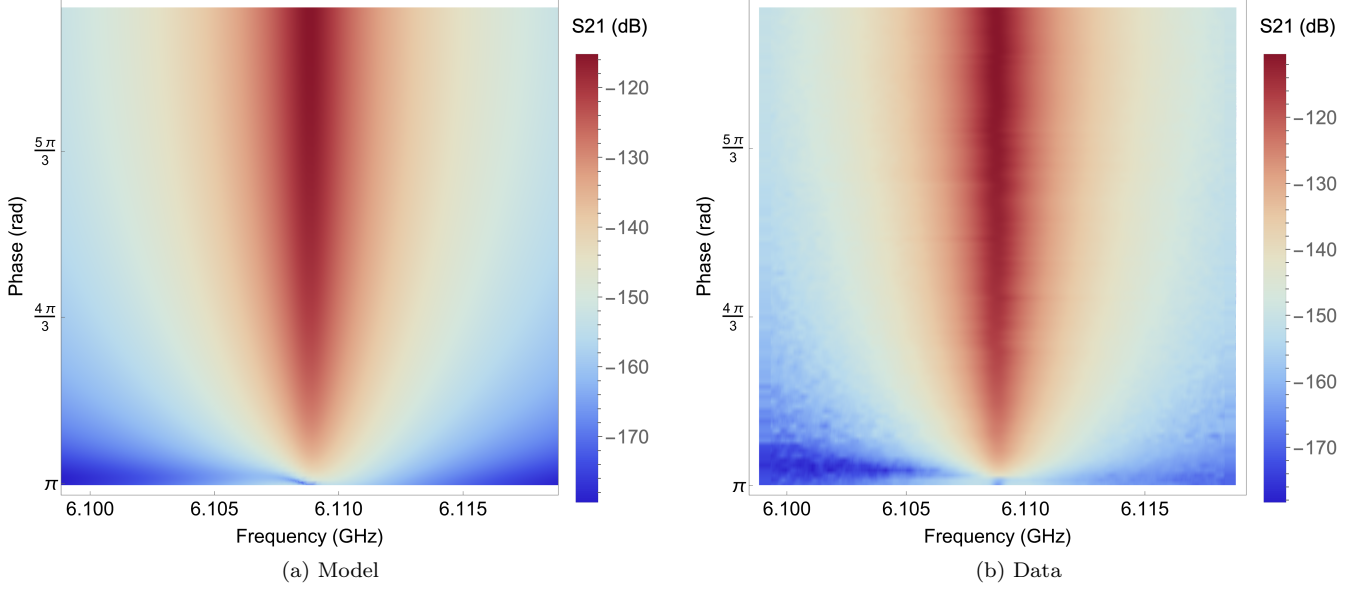


FIG. 4. Comparison between the simulated transfer function (using the parameters in Table I) for a near- π span of ϕ (left) and the interpolated 98 measured spectra (right). The absolute phase reference is arbitrary; therefore a constant phase offset was applied for visual alignment between model and data. Both plots are shown for the experimentally determined ϕ range.

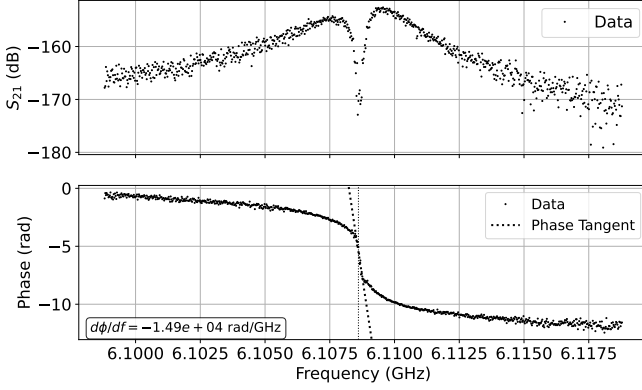


FIG. 5. Measured phase response near the balanced interference condition showing enhanced phase sensitivity. The local phase slope increases by nearly an order of magnitude relative to the near-resonant operating point shown in Fig. 3c, consistent with the behaviour expected near the antiresonance condition.

and 3, respectively:

$$\tilde{E}_n = Z_s \tilde{J}_{sn} + Z_t \tilde{J}_{s3}, \quad (11)$$

$$\tilde{E}_3 = Z_s \tilde{J}_{s3} + Z_t \tilde{J}_{sn}, \quad (12)$$

with surface currents \tilde{J}_{sn} and \tilde{J}_{s3} at sides n and 3, respectively, self impedance Z_s , at the two sides, and Z_t is the transfer impedance. The expression for Z_t is obtained from a transition boundary condition [30], which models a geometrically thin, but not electrically thin, sheet. To our knowledge, such a derivation is not readily available in the literature, and is thus provided in Appendix A.

Here, the self and transfer impedances are defined as

$$Z_s = -\frac{i\omega\mu}{k} \frac{1}{\tan(kd)}, \quad (13)$$

$$Z_t = -\frac{i\omega\mu}{k} \frac{1}{\sin(kd)}, \quad (14)$$

with propagation distance (or foil thickness) d . The plane wave propagation constant k , is given by $k = \omega\sqrt{(\epsilon + (\frac{\sigma}{i\omega}))\mu}$, with angular frequency ω , conductivity σ , and the media's permittivity and permeability ϵ and μ , respectively. Only the dissipative part contributes to mutual power transfer; therefore the real part of Z_t is retained.

The dissipated power Pd , is generally

$$Pd = \int \text{Re}(\tilde{E} \cdot \tilde{J}_s^*) dS, \quad (15)$$

which after substituting Eqs. 11 and 12 becomes

$$Pd = \int (Z_s |\tilde{J}_{sn}|^2 + Z_s |\tilde{J}_{s3}|^2 + 2\text{Re}(Z_t) \text{Re}(\tilde{J}_{sn} \tilde{J}_{s3}^*)) dS, \quad (16)$$

where the final term is the mutual dissipated power

$$Pd_{n3} = 2\text{Re}(Z_t) \int \text{Re}(\tilde{J}_{sn} \tilde{J}_{s3}^*) dS. \quad (17)$$

This can also be written as

$$Pd_{n3} = Y_{n3} \text{Re}(V_n V_3^*), \quad (18)$$

with the voltages V_n and V_3 at sides n and 3, respectively, and in terms of the mutual admittance Y_{n3} . Combining

Eq 17 and 18, we can solve for the mutual admittance

$$Y_{n3} = 2Re(Z_t) \frac{\int Re(\tilde{J}_{sn} \cdot \tilde{J}_{s3}^*) dS}{Re(V_n V_3^*)}. \quad (19)$$

Substituting the stored energy of the microwave resonator $U = \frac{C|V|^2}{2}$, with resonator capacitance C , and noting $V = |V|e^{i\phi}$ with phase ϕ , we can write the mutual admittance as

$$Y_{n3} = Re(Z_t) \sqrt{\frac{C_n C_3}{U_n U_3}} \frac{\int Re(\tilde{J}_{sn} \cdot \tilde{J}_{s3}^*) dS}{Re(e^{i(\phi_n - \phi_3)})}. \quad (20)$$

The subscripts of C , U , and ϕ refer to the resonator associated to that side. \tilde{J}_{sn} and \tilde{J}_{s3} can be related to the magnetic fields at their respective surfaces, giving

$$Y_{n3} = Re(Z_t) \sqrt{\frac{C_n C_3}{U_n U_3}} \frac{\int Re((\vec{n}_n \times \vec{H}_{tn}) \cdot (\vec{n}_3 \times \vec{H}_{t3})^*) dS}{Re(e^{i(\phi_n - \phi_3)})}, \quad (21)$$

with \vec{n}_n and \vec{n}_3 unit vectors normal to their respective side in the $\pm z$ directions. Near both sides of the foil, the tangential magnetic field of a cylindrical resonator operating in the TM_{010} is

$$\vec{H}_t = -E_0 \begin{pmatrix} 0 \\ i\omega\epsilon \frac{a}{\chi_{01}} J'_0\left(\frac{\chi_{01}r}{a}\right) \\ 0 \end{pmatrix} e^{i\phi}, \quad (22)$$

at a radius r , with electric field normalisation constant E_0 and cavity radius a for the respective resonator. \vec{H}_{tn} and \vec{H}_{t3} involve the microwave experimental parameters for their respective sides. J_m is the Bessel function of the m -th kind where the primed J'_m is the derivative, and χ_{mu} is the u -th root of the Bessel functions of the m -th kind. This mode has capacitance

$$C = \frac{\pi\epsilon_0 a^2 J_1(\chi_{01})^2}{h} \quad (23)$$

and stored energy

$$U = \frac{1}{2} \pi\epsilon_0 a^2 h E_0^2 J_1(\chi_{01})^2, \quad (24)$$

with cavity height h and permittivity of free space ϵ_0 . Since, in this case, the metallic foil couples the ends of two cylindrical resonators of different radii, the integral is computed over the smaller radius. Substituting Eqs. 22, 23 and 24 into 21 and using the integral

$$\int J'_0\left(\frac{\chi_{01}r}{a_n}\right) J'_0\left(\frac{\chi_{01}r}{a_3}\right) r dr = -\frac{r(a_n J_0\left(\frac{r\chi_{01}}{a_3}\right) J_1\left(\frac{r\chi_{01}}{a_n}\right))}{\left(\frac{a_n}{a_3} - \frac{a_3}{a_n}\right) \chi_{01}}, \quad (25)$$

the admittance becomes

$$Y_{n3} = -4\pi\omega^2 \epsilon^2 \frac{Re(Z_t) a_n^4 a_3 J_0\left(\frac{a_n \chi_{01}}{a_3}\right) J_1(\chi_{01})}{\chi_{01}^3 h_n h_3 (a_n^2 - a_3^2)}. \quad (26)$$

The subscript of the a and h terms refer the radii and height of the respective cavity. Solving the standard admittance matrix we can calculate the mutual resistance as

$$R_{n3} = \frac{1 \pm \sqrt{1 + 4Y_{n3}^2 R_n R_3}}{2Y_{n3}} \approx \frac{1}{Y_{n3}}, \quad (27)$$

with the approximation valid for $4Y_{n3}^2 R_n R_3 \ll 1$, indeed the case for the parameters shown in Table II and with frequencies around 6 GHz. R_n and R_3 are the parallel resistance of the respective resonator given by

$$R_k = \frac{h_k^2 \mu_0}{2\pi a_k (a_k + h_k) R_{surface} \epsilon_0 J_1(\chi_{01})^2}. \quad (28)$$

μ_0 is the permeability of free space, and $R_{surface}$ is the surface resistance $R_{surface} = \sqrt{\frac{\omega\mu_0\rho}{2}}$ with resistivity ρ . Thus, Eq. 27 combined with Eq's. 26 and 28 determines the mutual resistance across the foil connecting two resonators.

B. Calculated Values

The physical parameters of the experiment are shown in Table II. The foil thickness was verified using a micrometer. The resonator parameters in conjunction with a few physical constants can be plugged in to Eq. 27 to obtain an expected mutual resistance and thus coupling.

TABLE II. Physical constants and parameters of the experiment.

Parameter	Value
a_n	$(18.00 \pm 0.005) \times 10^{-3}$ m
a_2	$(18.75 \pm 0.005) \times 10^{-3}$ m
h_n	$(35.00 \pm 0.01) \times 10^{-3}$ m
h_2	$(38.64 \pm 0.01) \times 10^{-3}$ m
d	$(9 \pm 1) \times 10^{-6}$ m
ϵ_0	8.854×10^{-12} F/m
μ_0	$4\pi \times 10^{-7}$ H/m
ρ_{Cu}	1.68×10^{-8} Ω m
σ_{Cu}	5.96×10^7 S/m

The mutual resistance R_{n3} is calculated to lie in the range $R_{n3} \approx (1-51) \times 10^{11} \Omega$. The positive root of Eq. 27 is taken as the physical solution; at very small coupling the analytical expression may yield small negative values, so the magnitude is reported. This extremely large value is intuitively consistent with the parallel-circuit picture: only small current flows across the foil, so the resulting coupling is weak, when the foil thickness spans multiple skin depths. Recalling Eq. 6, and expressing the resonator resistance as $R_n = R_{0n} \beta_n$, the mutual coupling is calculated to lie in the range $\Delta_{n3} \approx (1-48) \times 10^{-6}$ when the estimated foil thickness of $(9 \pm 1) \mu\text{m}$ is considered. Comparing this with the experimentally fitted values of $\Delta_{13} = (5.00 \pm 0.01) \times 10^{-6}$ and $\Delta_{23} = (4.10 \pm 0.01) \times 10^{-6}$

shows good agreement within the expected uncertainty. Given the strong sensitivity of the coupling to foil thickness and other geometric parameters, agreement at this level constitutes successful verification of the model.

The remaining variation between the expected and measured coupling values likely arises from uncertainties in highly sensitive parameters, such as the foil thickness, where a difference of a few micrometres can result in an order-of-magnitude change in the coupling. The foil thickness is considered to be uniform for the purposes of the calculation. More precise measurements of foil thickness would further reduce this uncertainty. Additionally, the resonator parameters such as conductivity may vary due to oxidation and other cavity differences. Small variations in the resonator mode structures will also lead to variations in the calculated cavity resistances.

V. CONCLUSION

We develop an equivalent circuit model to describe the coupling between three microwave cavity resonators interconnected by thin metallic foils. By introducing mutual resistance terms, the model accurately reproduces the experimentally observed interference phenomena and anti-resonant behaviour. The derived coupling values agree with those extracted from the fitted transfer function, confirming the physical validity of resistive inter-cavity coupling.

This study demonstrates a previously unexplored cou-

pling mechanism between volumetric microwave resonators, arising purely from dissipative interaction across a continuous conductive interface. This new approach enables precise control of weak coupling and the formation of sharp anti-resonances, in contrast to traditional aperture-based and other established coupling methods.

The demonstrated model offers a robust foundation for the design of new resonator architectures in precision microwave experiments. Such resistive coupling mechanisms may be exploited in fundamental physics tests sensitive to phase and potential differences, including studies of the scalar Electric Aharonov-Bohm effect and related dark-sector interactions. Future work may involve testing different foil and mode geometries for enhanced, rather than destructive, coupling. Additionally, this phenomenon can be investigated at cryogenic temperatures. Collectively, these results provide a rigorous theoretical and experimental basis for employing metallic foil mutual resistance as a controllable coupling mechanism in multi-resonator microwave systems.

ACKNOWLEDGEMENTS

This work was funded by the ARC Centre of Excellence for Dark Matter Particle Physics, CE200100008, and by the Defence Science Centre, an initiative of the State Government of Western Australia.

We thank Eugene N. Ivanov for valuable assistance in experimental preparation.

-
- [1] E. Ivanov, M. Tobar, and R. Woode, *IEEE Transactions on Ultrasonics, Ferroelectrics, and Frequency Control* **45**, 1526 (1998).
 - [2] C. R. Locke, E. N. Ivanov, J. G. Hartnett, P. L. Stanwix, and M. E. Tobar, *Review of Scientific Instruments* **79**, 051301 (2008).
 - [3] H. Paik, D. I. Schuster, L. S. Bishop, G. Kirchmair, G. Catelani, A. P. Sears, B. R. Johnson, M. J. Reagor, L. Frunzio, L. I. Glazman, S. M. Girvin, M. H. Devoret, and R. J. Schoelkopf, *Physical Review Letters* **107**, 240501 (2011).
 - [4] M. Goryachev, W. G. Farr, D. L. Creedon, Y. Fan, M. Kostylev, and M. E. Tobar, *Phys. Rev. Appl.* **2**, 054002 (2014).
 - [5] A. Krasnok, P. Dhakal, A. Fedorov, P. Frigola, M. Kelly, and S. Kutsaev, *Applied Physics Reviews* **11**, 011302 (2024).
 - [6] A. Romanenko, R. Pilipenko, S. Zorzetti, D. Frolov, M. Awida, S. Belomestnykh, S. Posen, and A. Grassellino, *Physical Review Applied* **13**, 034032 (2020).
 - [7] J. Krupka, K. Derzakowski, M. Tobar, J. Hartnett, and R. G. Geyer, *Measurement Science and Technology* **10**, 387 (1999).
 - [8] D. L. Creedon, Y. Reshitnyk, W. G. Farr, J. M. Martinis, T. L. Duty, and M. E. Tobar, *Applied Physics Letters* **98**, 222903 (2011).
 - [9] C. R. H. McRae, H. Wang, J. Gao, M. R. Vissers, T. Brecht, A. Dunsworth, D. P. Pappas, and J. Mutus, *Review of Scientific Instruments* **91** (2020).
 - [10] D. M. Pozar, *Microwave engineering: theory and techniques* (John Wiley & sons, 2021).
 - [11] W. G. Farr, D. L. Creedon, M. Goryachev, K. Benmessai, and M. E. Tobar, *Phys. Rev. B* **88**, 224426 (2013).
 - [12] E. Albertinale, L. Balembois, E. Billaud, V. Ranjan, D. Flanigan, T. Schenkel, D. Estève, D. Vion, P. Bertet, and E. Flurin, *Nature* **600**, 434 (2021).
 - [13] J. Travesedo, J. O’Sullivan, L. Pallegoix, Z. W. Huang, P. Hogan, P. Goldner, T. Chanélière, S. Bertaina, D. Estève, P. Abgrall, D. Vion, E. Flurin, and P. Bertet, *Science Advances* **11**, eadu0581 (2025).
 - [14] D. G. Blair, E. N. Ivanov, M. E. Tobar, P. J. Turner, F. van Kann, and I. S. Heng, *Phys. Rev. Lett.* **74**, 1908 (1995).
 - [15] B. D. Cuthbertson, M. E. Tobar, E. N. Ivanov, and D. G. Blair, *Review of Scientific Instruments* **67**, 2435 (1996).
 - [16] M. Aspelmeyer, T. J. Kippenberg, and F. Marquardt, *Reviews of Modern Physics* **86**, 1391 (2014).
 - [17] E. N. Ivanov, D. Mouneyrac, J.-M. Le Floch, M. E. Tobar, and D. Cros, *Review of Scientific Instruments* **81**, 064702 (2010).
 - [18] P. L. Stanwix, M. E. Tobar, P. Wolf, M. Susli, C. R. Locke, E. N. Ivanov, J. Winterflood, and F. van Kann, *Phys. Rev. Lett.* **95**, 040404 (2005).
 - [19] M. Nagel, S. R. Parker, E. V. Kovalchuk, P. L. Stanwix,

- J. G. Hartnett, E. N. Ivanov, A. Peters, and M. E. Tobar, *Nature Communications* **6**, 8174 (2015).
- [20] J.-S. G. Hong and M. J. Lancaster, *Microstrip filters for RF/microwave applications* (John Wiley & Sons, 2004).
- [21] A. Castelli, L. Martinez, J. Pate, R. Chiao, and J. Sharping, *Journal of Applied Physics* **126** (2019).
- [22] J. D. Teufel, D. Li, M. S. Allman, K. Cicak, A. Sirois, J. D. Whittaker, and R. Simmonds, *Nature* **471**, 204 (2011).
- [23] A. Ben-Asher, A. I. Fernandez-Dominguez, and J. Feist, arXiv preprint arXiv:2510.11850 (2025).
- [24] M. T. Hatzon, E. N. Ivanov, J. F. Bourhill, M. Goryachev, and M. E. Tobar, *Physical Review Applied* **22**, 014081 (2024).
- [25] R. Das, Q. Zhang, A. Kandwal, and H. Liu, *IEEE Access* **7**, 5095 (2018).
- [26] Z. W. Swana, P. A. J. van Rensburg, and H. C. Ferreira, in *2015 IEEE International Symposium on Power Line Communications and Its Applications (ISPLC)* (IEEE, 2015) pp. 47–52.
- [27] M. E. Tobar and D. G. Blair, *IEEE transactions on microwave theory and techniques* **39**, 1582 (1991).
- [28] M. T. Hatzon, G. R. Flower, M. Goryachev, J. F. Bourhill, and M. E. Tobar, *Physical Review Applied* **23**, 024058 (2025).
- [29] M. T. Hatzon, G. R. Flower, M. Goryachev, J. F. Bourhill, and M. E. Tobar, *URSI Radio Science Letters* **7**, 24 (2025).
- [30] COMSOL AB, *Optics Module User Guide — Section 6.24*, accessed: 2025-09-16.
- [31] R. E. Collin, *Foundations for microwave engineering* (John Wiley & Sons, 2007).

Appendix A: Transition Boundary Condition Derivation

Across a thin material layer, the electric fields tangential to the surface on side 1 and side 2, E_{t1} and E_{t2} , respectively, are given by

$$\tilde{E}_{t1} = Z_s \tilde{J}_{s1} + Z_t \tilde{J}_{s2}, \quad (\text{A1})$$

$$\tilde{E}_{t2} = Z_t \tilde{J}_{s1} + Z_s \tilde{J}_{s2}. \quad (\text{A2})$$

Z_s and Z_t are the self and transfer impedances of the material layer, and J_{s1} and J_{s2} the surface current den-

sities on the two sides. This comes from the fact that the boundary condition due to a large conductivity allows us to generally write, with little error [31], $\tilde{E}_t = Z_m J_s$, where Z_m is the surface resistance. Solving for the surface currents in Eqs. A1 and A2, we arrive at [30]

$$\tilde{J}_{s1} = \frac{Z_s \tilde{E}_{t1} - Z_t \tilde{E}_{t2}}{Z_s^2 - Z_t^2}, \quad (\text{A3})$$

$$\tilde{J}_{s2} = \frac{Z_s \tilde{E}_{t2} - Z_t \tilde{E}_{t1}}{Z_s^2 - Z_t^2}. \quad (\text{A4})$$

Following the standard transition matrices one has

$$\begin{bmatrix} V_1 \\ I_1 \end{bmatrix} = \begin{bmatrix} \cosh(\gamma d) & Z_0 \sinh(\gamma d) \\ \frac{1}{Z_0} \sinh(\gamma d) & \cosh(\gamma d) \end{bmatrix} \begin{bmatrix} V_2 \\ I_2 \end{bmatrix} \quad (\text{A5})$$

and

$$\begin{bmatrix} V_1 \\ V_2 \end{bmatrix} = \begin{bmatrix} Z_{11} & Z_{12} \\ Z_{21} & Z_{22} \end{bmatrix} \begin{bmatrix} I_1 \\ I_2 \end{bmatrix}, \quad (\text{A6})$$

for voltages and currents V_n and I_n , respectively. Here, d is the propagation distance, and $\gamma = i\omega\sqrt{(\epsilon + \frac{\sigma}{\omega i})\mu}$ is the propagation constant (wave number) determined by the material permittivity, conductivity, and permeability. One can then solve for Z_s and Z_t by defining $Z_s = Z_{11}$ and $Z_t = -Z_{12}$ arriving at

$$Z_s = -iZ_0 \frac{1}{\tan(kd)}, \quad (\text{A7})$$

$$Z_t = -iZ_0 \frac{1}{\sin(kd)}, \quad (\text{A8})$$

setting $\gamma = ik$. Finally, the characteristic impedance is given by [31]

$$Z_0 = \sqrt{\frac{\mu}{\epsilon + \frac{\sigma}{i\omega}}}. \quad (\text{A9})$$

And thus, we have derived the transition boundary condition [30].